

# Development of a time projection chamber with a sheet-resistor field cage

Kentaro Miuchi<sup>1,\*</sup>, Tomonori Ikeda<sup>1</sup>, Hirohisa Ishiura<sup>1</sup>, Kiseki D. Nakamura<sup>1</sup>, Atsushi Takada<sup>2</sup>, Yasuhiro Homma<sup>1</sup>, Ko Abe<sup>3,4</sup>, Koichi Ichimura<sup>3,4</sup>, Hiroshi Ito<sup>1</sup>, Kazuyoshi Kobayashi<sup>3,4</sup>, Takuma Nakamura<sup>1</sup>, Ryuichi Ueno<sup>1</sup>, Takuya Shimada<sup>1</sup>, Takashi Hashimoto<sup>1</sup>, Ryota Yakabe<sup>1</sup>, and Atsuhiko Ochi<sup>1</sup>

<sup>1</sup>*Department of Physics, Graduate School of Science, Kobe University, 1-1 Rokkodai-cho, Nada-ku, Kobe, Hyogo 657-8501, Japan*

<sup>2</sup>*Division of Physics and Astronomy, Graduate School of Science, Kyoto University, Kitashirakawa-iwake-cho, Sakyo-ku, Kyoto, Kyoto 606-8502, Japan*

<sup>3</sup>*Kamioka Observatory, Institute for Cosmic Ray Research, the University of Tokyo, Higashi-Mozumi, Kamioka, Hida, Gifu 506-1205, Japan*

<sup>4</sup>*Kavli Institute for the Physics and Mathematics of the Universe (WPI), the University of Tokyo, 5-1-5 Kashiwanoha, Kashiwa, Chiba 277-8582, Japan*

\*E-mail: miuchi@phys.sci.kobe-u.ac.jp

Received February 28, 2019; Revised April 5, 2019; Accepted April 8, 2019; Published June 9, 2019

.....  
A new-concept time projection chamber (TPC) using a commercial resistive sheet, sheet-resistor micro-TPC (SR $\mu$ -TPC), has been developed and its performance measured. SR $\mu$ -TPC has the potential to create a more uniform electric field than conventional TPCs with resistor chains owing to its continuous sheet resistivity, and its production would be easier than that of conventional TPCs. The material used in this study, Achilles-Vynilas, was found to be thin, transparent, and have low radioactivity. A performance test with cosmic muons showed very promising results, including the demonstration of good tracking performance. This type of TPC field cage can offer an alternative for the widely used conventional field cages.  
.....

Subject Index     H11, H20

## 1. Introduction

Since the invention of the time projection chamber (TPC) in the 1970s by David Nygren [1], many types of TPCs have been widely used in various physics experiments to take advantage of their full 3D tracking ability. Large-scale ( $O(1\text{ m})$ ) TPCs have been developed for accelerator experiments (NA49 [2] and ALICE [3]) and neutrino physics (T2K [4]). Applications of the TPC were widened to rare-event-search experiments in the 2000s and double-phase liquid noble-gas TPCs, like LUX [5], PandaX-II [6], XENON1T [7], and DarkSide-50 [8], are leading the direct dark matter search experiments owing mostly to their particle identification powers. A spherical proportional chamber (NEWS-G) with a high-pressure gas has been developed for low-mass dark matter searching [9], as well as a liquid xenon TPC (EXO-200) for neutrinoless double beta decay search experiments [10]. Furthermore, low-pressure large-volume gaseous TPCs, such as DRIFT-IId [11], NEWAGE-0.3b [12], and MIMAC [13], have been developed for direction-sensitive dark matter search experiments aiming to detect the tracks of recoil nuclei.

Typical field cages for these TPCs consist of field-shaping electrodes (wires, metal plates, aluminized Mylars, etc.) with resistor chains to supply appropriate potential to the electrodes. The

**Table 1.** List of candidates for the field-cage material of the SR $\mu$ -TPC. Catalog specifications and measured sheet resistivities are listed as “spec.” and “meas.”, respectively. The catalog specification of the Semitron ESd is shown in units of volume resistivity.

Product name	Material	Size (shipped) [m <sup>2</sup> ]	Thickness [mm]	Sheet resistivity	
				spec.	meas. [ $\times 10^{10} \Omega/\square$ ]
Semitron ESd	Polyacetal	$0.3 \times 0.6$	6	$10^8\text{--}10^{10}$ ( $\Omega\text{m}$ )	1–10 (along 0.6 m)
Anti-static film	Polyolefin	$1 \times 200$	0.05	$< 10$	1–100
Anti-static PVC sheet	PVC	$1.37 \times 30$	0.3	1–10	$2.0 \pm 0.2$
Achilles-Vynilas	PVC	$1 \times 10$	0.2	10	$3.3 \pm 0.3$
DPF-arutoron	PVC	$1.83 \times 50$	0.1	51	$> 100$

electric fields were precisely calculated using finite-element methods so as to achieve a uniform electric field in the detection volume. Each electrode in a typical design was about 1 cm wide with a 0.5 cm spacing in the drift direction. In most cases, the electrodes were designed to have more than 50% occupancy so as to shield the ground-potential of the vessel, which would cause deterioration of the electric field. This design, however, causes some non-uniformity of the electric field near the field cage, roughly closer than the width of the electrode. It would be useful if a sheet resistor with continuous resistivity could be used as the electric-field-shaping material because it is expected to form a uniform electric field even in the vicinity of the field cage. Detector assembly is also expected to be relatively easy, and a low-background detector can be made without resistors or solders. Resistive materials with bulk or sheet resistivities have attracted attention for the development of micro-patterned gaseous detectors (MPGDs) in terms of discharge suppressions [14,15]. These materials are also widely used for anti-static purposes. In this paper, we report the development and performance measurements of a sheet-resistor micro-TPC, or SR $\mu$ -TPC.

## 2. Detector assembly

The material for the field cage of the SR $\mu$ -TPC was selected from several candidates. The required sheet resistivity was  $10^{10}\text{--}10^{11} \Omega/\square$  mainly because of the realistic high-voltage supply<sup>1</sup>. Several commercially available samples were purchased and their properties were measured. The measured material candidates are summarized in Table 1. The Semitron, used in Ref. [15], was in the form of a plate, while the others were sheets shipped in rolls. The sheet resistivities along the widths of the rolls were measured every 10 cm interval<sup>2</sup>. Two copper cubes ( $2 \times 2 \times 2 \text{ cm}^3$ ) separated by a distance of 2 cm, were used as electrodes for the sheet-resistivity measurement. A bias voltage of up to 1 V was supplied between the electrodes by a dry battery and the current was amplified by a homemade amplifier with a gain of 5 mV/pA. Texas Instruments TLC2652 operational amplifiers were used for the amplifier. The bias voltage and current voltage were read by multimeters (Hewlett Packard 34401A and Keithley 2000 multimeters, respectively) and recorded by a computer. This

<sup>1</sup> A field cage made of a material with a sheet resistivity of  $10^{10} \Omega/\square$  for a 1 m drift length and 1 m diameter has a resistivity of  $3 \times 10^9 \Omega$ , which requires a current of 10  $\mu\text{A}$  for a 30 kV voltage.

<sup>2</sup> This was to ensure that there existed at least one direction with a good uniformity that could be used for the drift direction.

**Table 2.** Measurement results with the HPGe. The values are shown in units of mBq/kg. Radioactivities of a typical resistor (KTR10EZPF, taken from Ref. [16] and renormalized) are shown for reference.  $^{226}\text{Ra}$  and  $^{228}\text{Ra}$  are the isotopes in the  $^{238}\text{U}$  chain and  $^{232}\text{Th}$  chain, respectively.

	$^{226}\text{Ra}$ ( $^{238}\text{U}$ chain)	$^{228}\text{Ra}$ ( $^{232}\text{Th}$ chain)	$^{40}\text{K}$	$^{60}\text{Co}$
Achilles-Vynilas	< 18.4	< 7.77	< 112	< 2.54
Resistor KTR10EZPF	$(4.1 \pm 0.5) \times 10^2$	$(4.3 \pm 0.5) \times 10^2$	$(4.2 \pm 0.6) \times 10^3$	< 25

system was confirmed to be able to measure up to  $1.0 \times 10^{11} \Omega$  with a precision of 1% using a standard high-precision resistor.

Catalog specifications and the measurement results are listed in Table 1. The error of the sheet resistivity is the standard deviation of the measured resistivities. For the samples whose measured sheet resistivity varied by more than one order of magnitude, the results are shown with “–” to indicate the orders. The DPF-arutoron showed a resistivity larger than the range of our system, so the lower limit is shown. In terms of the uniformity of the sheet resistivity, two samples, namely anti-static PVC (polyvinyl chloride) and Achilles-Vynilas, were found to be relatively good candidates. It should be noted that the uniformity does not greatly affect the practical use as an anti-electric material; thus, it is understandable that there was a large variety in uniformity between the measured products. Anti-static PVC was found to have a resistivity difference on a large scale of about 15%/m while that of Achilles-Vynilas was less than 1%/m. Achilles-Vynilas was thus selected as the best material among the candidates. One interesting property of this material, which may broaden its application, was that a transmittance of more than 90% was guaranteed for visible light with a wave length of  $> 450 \text{ nm}$ .

The radioactive contamination of the Achilles-Vynilas was measured to ensure its viability for rare-event-search experiments. A high-purity germanium detector (HPGe) at the Kamioka observatory in the Kamioka Mine (2700 m water equivalent) was used. Details of the detector system can be found in Ref. [16]. The results are summarized in Table 2. No finite value was detected and upper limits at 90% C.L. are shown in Table 2. Radioactivities of resistors listed in Ref. [16] are also shown in Table 2 for reference. Typical amounts needed for a  $10 \times 10 \times 10 \text{ cm}^3$ -sized TPC are  $O(10 \text{ g})$  and  $O(0.1\text{--}1 \text{ g})$  in the case of the resistive sheet and resistor chains, respectively. Upper limits obtained here indicate a promising potential of using this material for rare-event-search experiments. The  $\alpha$ -ray emission rate was also measured with an  $\alpha$ -ray detector described in Ref. [17] and the upper limit at 90% C.L. was  $2.4 \times 10^{-2} \alpha/\text{h}/\text{cm}^2$ . The  $\alpha$ -ray emission rate was less than that of the  $\mu$ -PIC  $\left(\left(3.57_{-0.33}^{+0.35}\right) \times 10^{-1} \alpha/\text{h}/\text{cm}^2\right)$  described in Ref. [17]. Dedicated measurements would be needed to confirm the requirement for each individual experiment.

A sheet-resistor field cage was made with Achilles-Vynilas. A photograph and schematic drawings of the SR $\mu$ -TPC are shown in Figs. 1 and 2, respectively. The field cage was built by combining four acrylic plates as “walls” and a steel mesh as a “drift top”. The size of each acrylic plate was  $80 \times 140 \times 10 \text{ mm}^3$ . The resistive sheets were attached to the inner area of the acrylic plate by thermal pressing at a temperature at which the acrylic became soft but the properties of the resistive sheet were not affected. The drift-top and drift-bottom parts of the resistive sheet were sandwiched by copper plates with a thickness of 1 mm. These electrodes were screwed into each other so that the ohmic contact to the resistive sheet was secured. The inner size of the field cage was  $130 \times 130 \text{ mm}^2$  and the drift length was 85 mm. The field cage was then coupled with the GEM +  $\mu$ -PIC gas-detector system. The GEM (made by Scienergy) was made of liquid crystal polymer with a thickness of

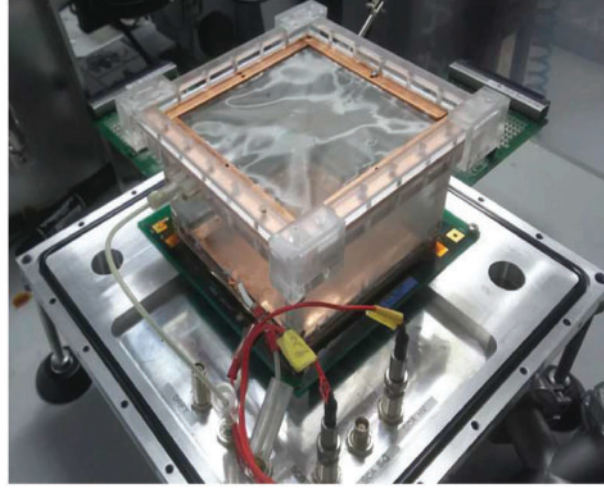


**Fig. 1.** Photograph of the SR $\mu$ -TPC. Sheet resistors are attached to the inner plane of the four walls made of acrylic.

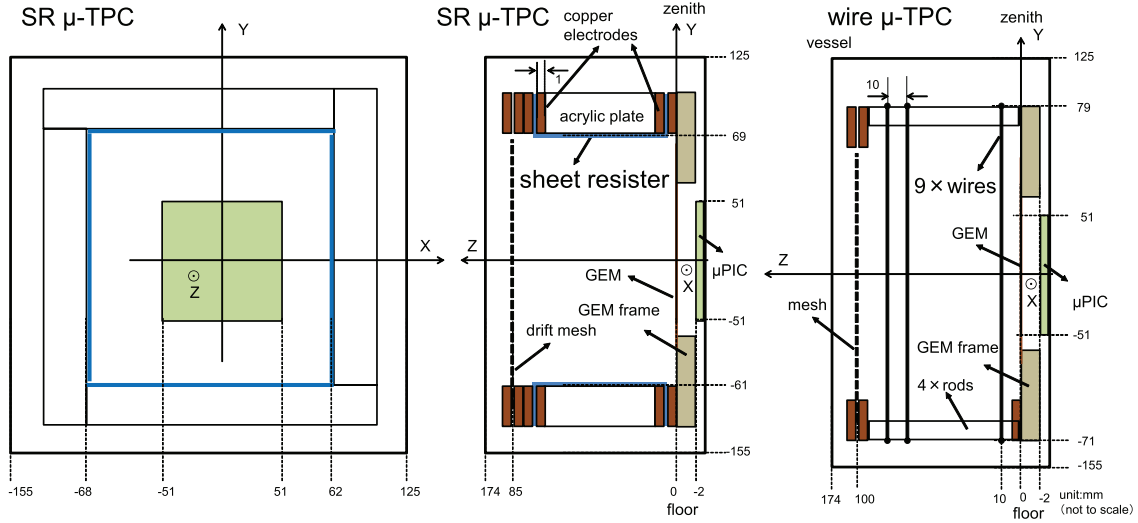


**Fig. 2.** Schematic drawings of the SR $\mu$ -TPC and the wire  $\mu$ -TPC. Side views of the SR $\mu$ -TPC and side view of wire  $\mu$ -TPC are shown on the left (from drift-top), center (from drift-side), and right (from drift-side), respectively. Please note that these drawings are not to scale.

100  $\mu\text{m}$ , a hole diameter of 70  $\mu\text{m}$ , and a hole pitch of 140  $\mu\text{m}$ . The GEM was used as the first-stage gas amplifier. The  $\mu$ -PIC was a 2D readout device with orthogonally placed strips with a pitch of 400  $\mu\text{m}$ . The charge from each strip was digitized by an amplifier-shaper-discriminator (ASD) chip [18] and synchronized with a field-programmable-gate-array (FPGA)-based electronics board with a system frequency of 100 MHz. The start time and duration of the discriminated signal from each strip were recorded. Here the time reference was provided by an external trigger. The  $\mu$ -PIC system thus recorded 2D images on two planes. Details of the gas-detector system, with the difference in the detector size, can be found in Ref. [12]. The gas-amplification area of the GEM and the detection area of the  $\mu$ -PIC were  $100 \times 100 \text{ mm}^2$  and  $102 \times 102 \text{ mm}^2$ , respectively. The detection volume of the SR $\mu$ -TPC was thus  $100 \times 100 \times 85 \text{ mm}^3$ . The origin of the coordination system was set at the center of the GEM so that the  $XY$  plane corresponded to the readout plane of the  $\mu$ -PIC and

the  $Z$  axis corresponded to the drift direction. An existing field cage made of wire electrodes, wire  $\mu$ -TPC, was used for performance comparison. A schematic drawing of the wire  $\mu$ -TPC is shown in the right panel of Fig. 2. The inner size of the field cage was  $150 \times 150 \text{ mm}^2$  and the drift length was 100 mm. Due to the design of the  $\mu$ -PIC board, the centers of the field cage and the detection area were not aligned perfectly; there were offsets of 3 mm and 4 mm in the  $X$  and  $Y$  directions, respectively. The largest distance between the sheet-resistor field cage and the detection area was 18 mm ( $= 69 - 51 \text{ mm}$ , shown in the  $+Y$  area), as seen in the center drawing of Fig. 2, while that of the wire field cage was 29 mm. The tracking performances of the SR $\mu$ -TPC and wire  $\mu$ -TPC in regions more than 20 mm and 30 mm away from the field cage were studied with these detectors.

### 3. Performance test

Performance tests of the SR $\mu$ -TPC and wire  $\mu$ -TPC were conducted using cosmic-ray muons. The chamber was filled with a gas mixture of argon (0.88 bar) and ethane (0.12 bar) and operated with a total gas gain of  $4.0 \times 10^4$ . A drift field of 0.2 kV/cm was formed. The  $XZ$  plane was set horizontally and the  $Y$  axis was aligned vertically as shown in Fig. 2. A coincidence of two plastic scintillators was used for the trigger. Both scintillators were placed above the TPC chamber for the SR $\mu$ -TPC measurement ( $Y = 130 \text{ mm}$  and  $170 \text{ mm}$ ) while one was set below the TPC for the wire  $\mu$ -TPC measurement ( $Y = -185 \text{ mm}$  and  $170 \text{ mm}$ )<sup>3</sup>. The measurement periods after the gas filling were 0.2–0.32 d for the SR $\mu$ -TPC and 0.1–0.52 d for the wire  $\mu$ -TPC.

Track events for the analysis were selected from the total event samples. Low-energy events below 5 keV were rejected in order to exclude noise events. The energy spectrum of the muon events peaked at 30 keV. Tracks with lengths between 7 cm and 15 cm were selected in order to exclude potential systematic error due to the trigger condition difference. After these event selections, the event rates were  $(2.6 \pm 0.2) \times 10^{-2} \text{ [events/s]}$  and  $(2.3 \pm 0.1) \times 10^{-2} \text{ [events/s]}$  for the SR $\mu$ -TPC and wire  $\mu$ -TPC, respectively. These rates were consistent within  $2\sigma$  and the muon tracks with same properties were selected for the analysis.

A typical muon event detected with the  $\mu$ -PIC system is shown in Fig. 3. The discriminated signal of each strip is shown by a pink mark in Fig. 3. The representative hit-timing ( $T$ ) for each strip was determined at 20% of the signal duration from the beginning of the signal and it is shown with a red mark<sup>4</sup>.  $T$  was used to calculate  $Z$  based on the time from the trigger and the drift velocity (4.5 cm/ $\mu$ s, measured by the full-drift length hits). Hereafter, this set of ( $X, Z$ ) or ( $Y, Z$ ) is referred to as a “hit”. The hits were fitted with straight lines independently in the  $XZ$  and  $YZ$  planes. Best-fit results are shown with the green lines in Fig. 3. Each hit has measured 2D coordinates ( $XZ$  or  $YZ$ ) and the position of the third coordinate ( $Y$  or  $X$ ) was calculated by the  $Z$  value and the line on the other plane so that each hit had a 3D position. The ( $X, Y$ ) position was used to categorize each hit into the “inner” or “outer” region in order to evaluate the effect of the distance from the field cage. Here the inner region was defined as the area that is at least 3.5 cm away from the field cage for both the SR $\mu$ -TPC and the wire  $\mu$ -TPC. This boundary was determined so that similar numbers of hits were expected in both outer and inner regions in total. The inner and outer boundaries of the SR $\mu$ -TPC are shown in Fig. 3 with dashed lines.

<sup>3</sup> Measurements with the same trigger conditions were performed but the gas conditions were found to differ so these two data-sets were used for the analysis.

<sup>4</sup> This method was modified from the one introduced in Ref. [19].

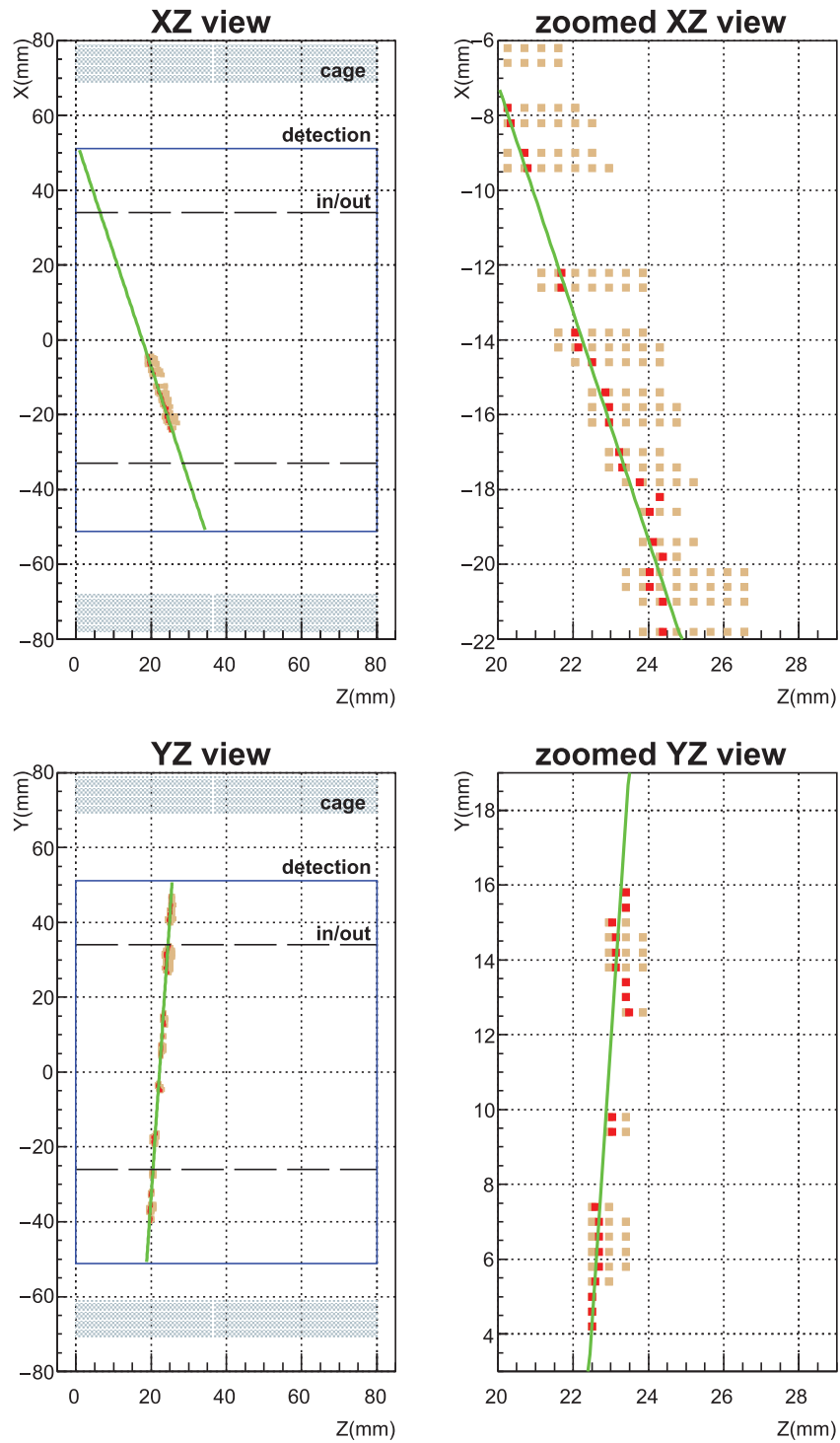


**Fig. 3.** A typical muon event taken by the SR $\mu$ -TPC. The upper and lower figures show the tracks in the XZ (top-view) and YZ (side-view) planes, respectively. The right figures show zoomed images of the same event. The pink marks are the discriminated signals from each strip and the red marks show the hits. The green lines show the best-fit lines. The gray parts indicate the TPC cages. The solid and dashed lines represent the detection volume and boundary of the inner and outer regions, respectively.



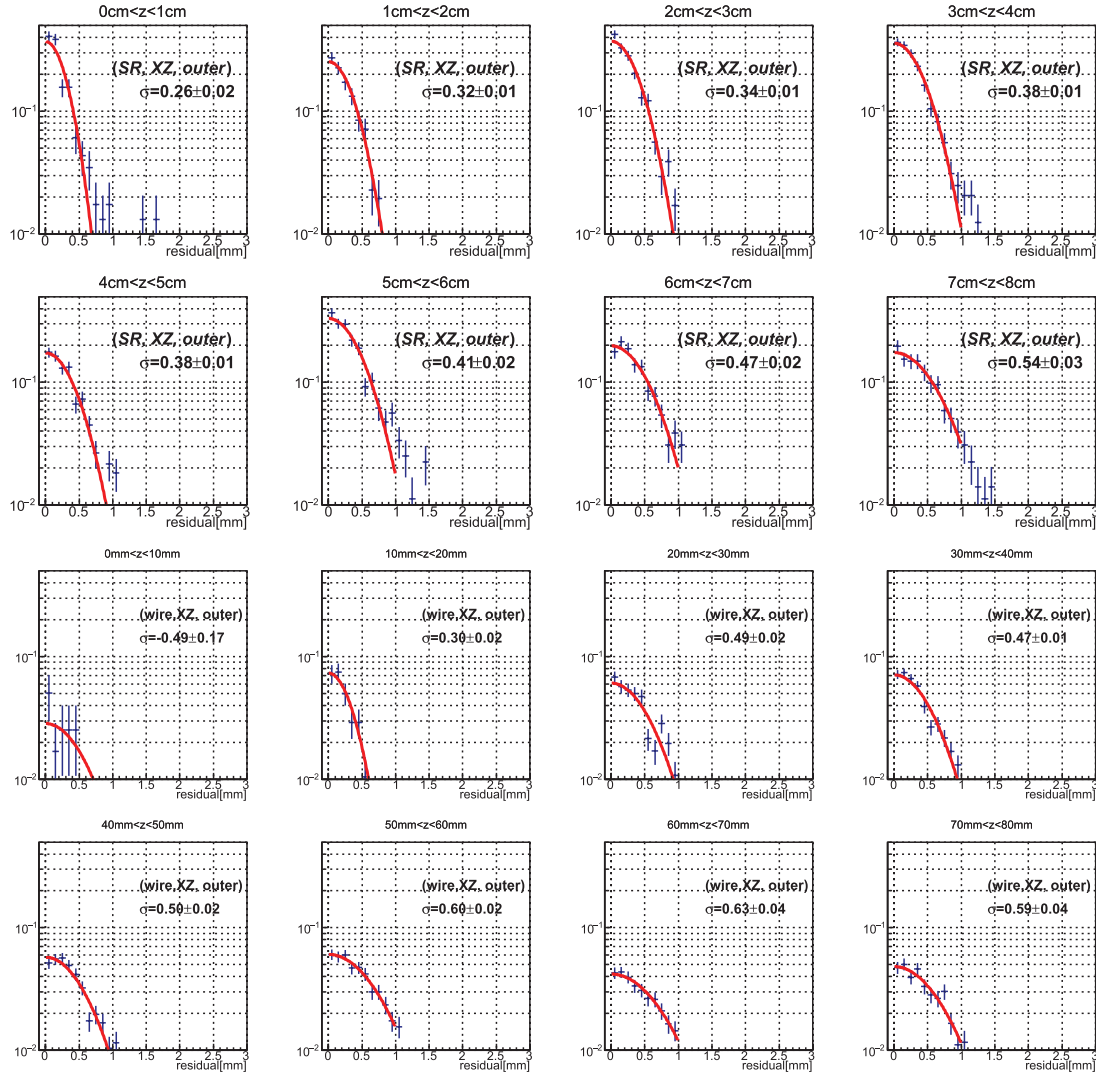


**Fig. 4.** The residual distributions of the (SR, XZ, outer) (upper) and (wire, XZ, outer) (lower) data.

Residuals were calculated as the distance of a hit and the best-fit line in each plane. According to the combinations of (SR or wire)  $\times$  (XZ or YZ)  $\times$  (inner or outer), the data were independently analyzed and compared. The combination is labeled as (SR, XZ, inner) for hits in the inner region analyzed on the XZ plane taken with the SR $\mu$ -TPC and for other combinations in the same manner. Typical residual distributions of the (SR, XZ, outer) and (wire, XZ, outer) data are shown in Fig. 4. Here the events are classified according to Z or the drift distance. Each residual distribution was fitted with a Gaussian function whose mean was fixed at 0. The height and the  $\sigma$  were treated as free parameters. The results of the fitting are also shown in Fig. 4 with red lines. The  $\sigma$  of each distribution can be represented as Eq. (1):

$$\{\sigma_{i,j,k}(Z)\}^2 = \{\sigma_{\text{dd},(i,j,k)}\}^2 + \{\sigma_{\text{diff},(i,j,k)}(Z)\}^2. \quad (1)$$

Here,  $i$  = SR or wire is the field-cage type,  $j$  = XZ or YZ is the detection plane, and  $k$  = inner or outer is the region of interest.  $\sigma_{\text{dd}}$  comprises the detector-intrinsic and drift-field-dependent

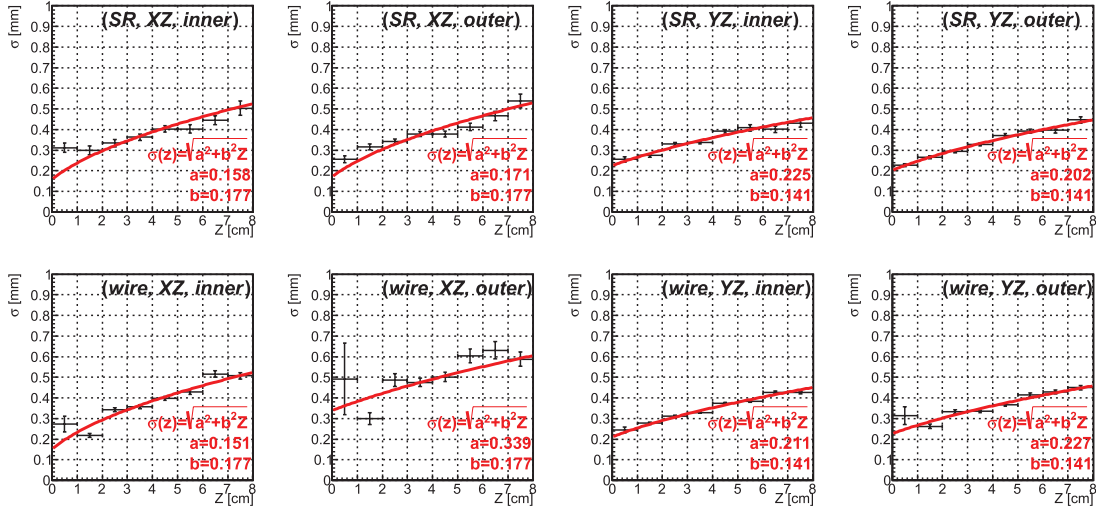


Fig. 5.  $\sigma$  dependence on  $Z$  for eight data-sets.

position resolutions and is  $Z$ -independent.  $\sigma_{\text{diff}}$  is a diffusion-related term that has a  $Z$  dependence as Eq. (2):

$$\sigma_{\text{diff},(i,j,k)}(Z) = d'_j \sqrt{Z}, \quad (2)$$

where  $d'_j$  is the effective diffusion in mm at  $Z = 1$  cm. Since the effective number of primary electrons for the determination of one hit point is in practice more than one, the measured  $d'_j$  parameters are better than the diffusion values defined by the expected position for a single electron. It should be noted that  $\sigma_{\text{diff}}$  basically depends upon the electron diffusion in the gas and is therefore independent of the field-cage type  $i$  and position  $k$ . The dependence on  $j$  still remains, owing to the track directions. For the  $YZ$  plane case, transverse diffusion, which is in the  $Y$ -axis direction, may be observed smaller than the original size because most of the track directions are also in the  $Y$ -axis directions. This effect is also quantitatively treated in the next section.

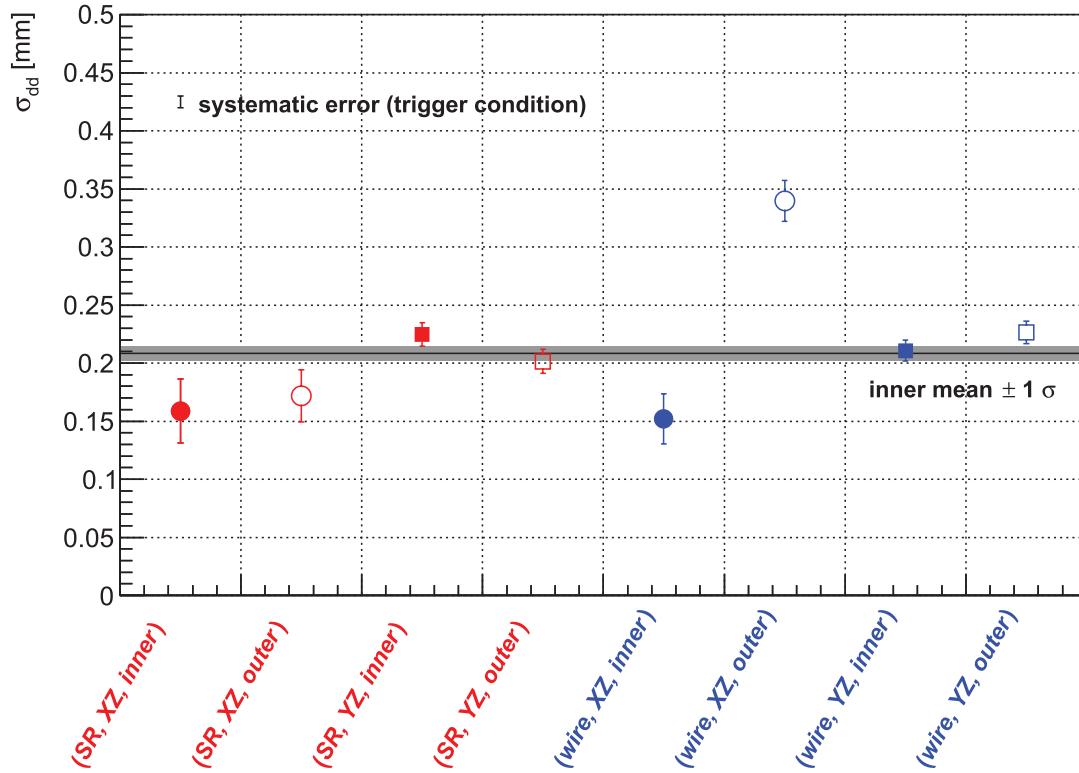
$\sigma$  parameters derived from the fitting of the distributions of the residuals were plotted as a function of  $Z$  and are shown in Fig. 5. There, eight results corresponding to eight data-sets are all shown. All of the data (64 bins) were simultaneously fitted with Eq. (1). Here, 10 (8 for  $\sigma_{\text{dd},(i,j,k)} + 2$  for  $d'_j$ ) free parameters were used. The results are shown with red lines and characters in Fig. 5 and also in Table 3. The  $\chi^2/\text{NDF}$  of the fitting was 60.2/54. The obtained  $\sigma_{\text{dd}}$  values are shown in Fig. 6. There, the eight conditions are labeled below the data. The size of the systematic error due to the difference of the trigger condition is indicated with a solid line in the top-left corner; this will be discussed in the following section.

The primary result of this work is that the  $\text{SR}\mu\text{-TPC}$  actually worked. This is demonstrated by Fig. 3 and the SR data in Fig. 6 being comparable to the (wire, inner) data. Thus, it can be said that no significant differences between (SR, XZ, inner) and (SR, XZ, outer), (SR, YZ, inner) and (SR, YZ, outer) were seen. This means that a good performance was kept at the outer region (20 mm from the field cage) of the  $\text{SR}\mu\text{-TPC}$ . The mean of the inner data and their  $1\sigma$  band are shown by the solid line and gray band for reference. No significant differences were observed between the (SR, outer) data and the inner mean. This result is highlighted when the (wire, XZ, outer) result is compared with other data. The result was significantly larger than the others, indicating that the electric field of



**Table 3.** Fit results for  $\sigma_{dd,(i,j,k)}$  and  $d'_j$ . The units are mm for  $\sigma_{dd,(i,j,k)}$  and mm/ $\sqrt{\text{cm}}$  for  $d'_j$ .

Parameter	Best-fit value
$\sigma_{dd,(SR,XZ,inner)}$	$0.158 \pm 0.043$
$\sigma_{dd,(SR,XZ,outer)}$	$0.171 \pm 0.031$
$\sigma_{dd,(SR,YZ,inner)}$	$0.225 \pm 0.013$
$\sigma_{dd,(SR,YZ,outer)}$	$0.202 \pm 0.013$
$\sigma_{dd,(wire,XZ,inner)}$	$0.151 \pm 0.035$
$\sigma_{dd,(wire,XZ,outer)}$	$0.339 \pm 0.021$
$\sigma_{dd,(wire,YZ,inner)}$	$0.211 \pm 0.013$
$\sigma_{dd,(wire,YZ,outer)}$	$0.227 \pm 0.013$
$d'_{XZ}$	$0.177 \pm 0.007$
$d'_{YZ}$	$0.141 \pm 0.003$

**Fig. 6.** Obtained  $\sigma_{dd}$ . Red and blue markers show SR $\mu$ -TPC and wire  $\mu$ -TPC results, respectively. Circles and squares show XZ and YZ results, respectively. Filled and open markers show the inner and outer results, respectively.

the wire  $\mu$ -TPC was deteriorated due to the ground voltage of the vessel seen through the wires. The (wire, XZ, inner), on the other hand, showed a result consistent with the other data, confirming that there was no systematic problem for the (wire, XZ) setup. The comparison of (SR, XZ, outer) and (wire, XZ, outer) illustrates that the sheet-resistor field cage was useful for shielding the potential of the vessel. The difference between (wire, XZ, outer) and (wire, YZ, outer) could be due to the track direction and the diffusion, which will be discussed in Sect. 4.

#### 4. Discussion

Our measurements indicate promising results for the performance of the SR $\mu$ -TPC. Although the comparison-based results discussed in Sect. 3 were robust and reliable, some discussion is important to confirm the consistency and correctness of all the measurements.

First, as summarized in Table 3, the measured effective diffusion on the XZ plane ( $d'_{XZ} = 0.177 \pm 0.007$ ) was larger than that on the YZ plane ( $d'_{YZ} = 0.141 \pm 0.003$ ). This result can be explained by the following discussion. The transverse and longitudinal diffusions,  $d_t$  and  $d_l$ , calculated with the MAGBOLTZ 11.6 simulation [20], were  $0.48 \text{ mm}/\sqrt{\text{cm}}$  and  $0.29 \text{ mm}/\sqrt{\text{cm}}$ , respectively. Here the transverse diffusion can be observed as the diffusions along the  $X$  and  $Y$  axes and the longitudinal one can be seen as the diffusion along the  $Z$  axis. It should be noted that when the diffusions are measured using long tracks the diffusions along the track directions are not observed; only the diffusions perpendicular to the track can be observed. This effect can be written as Eqs. (3)–(4):

$$(d_{XZ}(\phi))^2 = (d_t \sin \phi)^2 + (d_l \cos \phi)^2 \quad (3)$$

$$(d_{YZ}(\theta))^2 = (d_t \sin \theta)^2 + (d_l \cos \theta)^2, \quad (4)$$

where  $d_{XZ}(\phi)$  and  $d_{YZ}(\theta)$  are the observable diffusions on the XZ and YZ planes, respectively.  $\phi$  and  $\theta$  are the angles between the track and the  $X$  and  $Y$  axes, respectively. The detector was set so that  $\phi$  was the azimuth angle and  $\theta$  was the zenith angle. The weighted means of Eqs. (3) and (4),  $d_{XZ}$  and  $d_{YZ}$ , were calculated by simulation taking account of the detector geometry and the zenith angle dependence of the cosmic muon. The obtained values were  $d_{XZ} = 0.39 \text{ mm}/\sqrt{\text{cm}}$  and  $d_{YZ} = 0.32 \text{ mm}/\sqrt{\text{cm}}$ . These observable diffusions were related to effective diffusions as Eqs. (5)–(6):

$$d'_{XZ} = d_{XZ}/\sqrt{N_{XZ}} \quad (5)$$

$$d'_{YZ} = d_{YZ}/\sqrt{N_{YZ}}, \quad (6)$$

where  $N_{XZ}$  and  $N_{YZ}$  are the effective numbers of electrons for the determination of each hit point in the XZ and YZ planes, respectively. The result can be explained with  $N_{XZ} \sim N_{YZ} \sim 5$ . The difference between  $\sigma_{\text{dd},(\text{wire},XZ,\text{outer})}$  and  $\sigma_{\text{dd},(\text{wire},YZ,\text{outer})}$  can be understood in the same way; smaller values are obtained for the position displacement along the track direction ( $Y$  axis) than that along the  $X$  axis. In this case, the measured values can be explained with  $\sigma_{\text{drift},(\text{wire},Z,\text{outer})} = 0.1 \text{ mm}$  and  $\sigma_{\text{drift},(\text{wire},XY,\text{outer})} = 0.5 \text{ mm}$ , where  $\sigma_{\text{drift},(\text{wire},Z,\text{outer})}$  and  $\sigma_{\text{drift},(\text{wire},XY,\text{outer})}$  are standard deviations of the position displacements by the drift-field distortion in the  $Z$  direction and  $XY$  plane, respectively. Precise calculation of the electric field in future work would provide a more quantitative explanation.

Here it has been shown that the track direction affected the  $\sigma$  results. Therefore, the trigger condition difference between the two measurements could cause systematic errors although the track-length cut provided a good event selection in terms of the event rate. A parameter,  $\Delta X$ , the difference between the maximum and minimum  $X$  positions in the hits in a track, was used to evaluate the systematic error because this parameter represents the track direction. The mean values of  $\Delta X$  of the selected events in the two measurements,  $\overline{\Delta X}(\text{SR})$  and  $\overline{\Delta X}(\text{wire})$ , were  $1.6 \text{ cm}$  and  $1.4 \text{ cm}$ , respectively. When the events with  $\Delta X > 3 \text{ cm}$  were excluded from the SR data,  $\overline{\Delta X}(\text{SR})$  was  $1.3 \text{ cm}$ , which was smaller than  $\overline{\Delta X}(\text{wire})$ . The difference of the  $\sigma_{\text{dd},(\text{SR})}$  between the original result and the one with this additional cut was treated as a systematic error and is indicated in Fig. 6. The systematic error due to the trigger condition difference was confirmed to be smaller than the statistical errors and was found not to affect the conclusions of this work.

Second, it would be interesting to know if a drift-field-dependent term can be separated from the detector-intrinsic one since the results shown in Table 3 are all convoluted values. After some trials, this data-set was found to be insufficient to give any conclusive results on the drift-field-dependent term.

Finally, let us discuss the remaining studies that need to be done on SR $\mu$ -TPC before practical use in a large-scale TPC. The tracking performance in the area 20 mm or more away from the field cage was confirmed. One of the potential advantages of SR $\mu$ -TPC is that there would be less electric-field deterioration near the wall than with a ring-type or tape-type TPC. A dedicated field cage with the same or smaller area compared to the detection area would help with a further study on this potential. Long-term stability is also of particular interest, since rare-event-search experiments usually require stable measurements on the order of years. Another interesting study is the use in cryogenic systems for liquid-noble-gas TPCs. Unfortunately, this particular product (Achilles-Vynilas) showed a semiconductor-like temperature dependence ( $\propto \exp(-1.5 \times 10^4 \text{ T})$ ) at room temperature. It is thus expected that the resistivity would be too high at temperatures below 100 K, which suggests that it is necessary to find another material. The resistive material for MPGDs would be a solution for the cryogenic version of SR $\mu$ -TPC<sup>5</sup>.

## 5. Conclusion

A new-concept TPC using a commercial resistive sheet, SR $\mu$ -TPC, was developed and its performance was measured. With a sheet resistor, SR $\mu$ -TPC has the potential to make a more uniform electric field than conventional TPCs with resistor chains. Detector assembly was easier than that of conventional TPCs. The material used in this study, Achilles-Vynilas, was found to be thin, transparent, and have low radioactivity. The tracking-performance measurement with cosmic muons showed very promising results, indicating that this type of field cage actually works and shows good tracking performance even in the volume close to (20 mm away from) the field cage. This type of TPC field cage offers an alternative for the widely used conventional field cages.

## Acknowledgements

We gratefully acknowledge the cooperation of Kamioka Mining and Smelting Company. We thank the XMASS Collaboration for their help on the low-background measurement technologies. This work was supported by the Japanese Ministry of Education, Culture, Sports, Science and Technology, a Grant-in-Aid for Scientific Research, ICRR Joint-Usage, Japan Society for the Promotion of Science (JSPS) KAKENHI Grant Numbers 16H02189, 26104004, 26104005, 26104009, and the JSPS Bilateral Collaborations (Joint Research Projects and Seminars) program.

## References

- [1] J. N. Marx and D. R. Nygren Phys. Today **31**, 46 (1978).
- [2] S. Afanasiev et al. [NA49 Collaboration], Nucl. Instrum. Meth. A **430**, 210 (1999).
- [3] J. Alme et al., Nucl. Instrum. Meth. A **622**, 316 (2010).
- [4] N. Abgrall et al., Nucl. Instrum. Meth. A **637**, 25 (2011).
- [5] D. S. Akerib et al., Nucl. Instrum. Meth. A **704**, 111 (2013).
- [6] A. Tan et al. [PandaX-II Collaboration], Phys. Rev. D **93**, 122009 (2016).
- [7] E. Aprile et al. [XENON Collaboration], Eur. Phys. J. C **77**, 881 (2017).
- [8] P. Agnes et al., Phys. Lett. B **743**, 456 (2015).
- [9] Q. Arnaud et al., Astropart. Phys. **97**, 54 (2018).

<sup>5</sup> There was a report after the submission of this work on a “resistive shell liquid argon TPC” [21].

- [10] M. Auger et al., J. Instrum. **7**, P05010 (2012).
- [11] J. B. R. Battat et al., Astropart. Phys. **91**, 65 (2017).
- [12] K. Nakamura et al., Prog. Theor. Exp. Phys. **2015**, 043F01 (2015).
- [13] D. Santos et al., J. Phys.: Conf. Ser. **460**, 012007 (2013).
- [14] T. Alexopoulos, J. Burnens, R. de Oliveira, G. Glonti, O. Pizzirusso, V. Polychronakos, G. Sekhniadze, G. Tsipolitis, and J. Wotschack, Nucl. Instrum. Meth. A **640**, 110 (2011).
- [15] A. Rubin, L. Arazi, S. Bressler, L. Moleri, M. Pitt, and A. Breskin, J. Instrum. **8**, P11004 (2013).
- [16] K. Abe et al. [XMASS Collaboration], Nucl. Instrum. Meth. A **922**, 171 (2019).
- [17] H. Ito, T. Hashimoto, K. Miuchi, K. Kobayashi, Y. Takeuchi, K. D. Nakamura, T. Ikeda, and H. Ishiura, submitted to Nucl. Instrum. Meth. A, [arXiv:1903.01090](https://arxiv.org/abs/1903.01090) [physics.ins-det] [[Search INSPIRE](#)].
- [18] O. Sasaki and M. Yoshida, IEEE Trans. Nucl. Sci. **46**, 1871 (1999).
- [19] S. Komura, Improvement of the tracking algorithm for the electron tracking Compton camera. *Master Thesis*, Kyoto University (2013).
- [20] R. Veenhof, J. Instrum. **4**, P12017 (2009).
- [21] R. Barner et al., Instruments **3**, 28 (2019) [[arXiv:1903.11858](https://arxiv.org/abs/1903.11858) [physics.ins-det]] [[Search INSPIRE](#)].